Geophysical Journal International

Directionality of Ambient Noise in the Mississippi Embayment

Journal:	*Geophysical Journal International*
Manuscript ID	Draft
Manuscript Type:	Research Paper
Date Submitted by the Author:	n/a
Complete List of Authors:	Liu, Chunyu; University of Memphis, Center for Earthquake Research and Information Langston, Charles; University of Memphis, Center for Earthquake Research and Information Aslam, Khurram; University of Memphis, Center for Earthquake Research and Information
Keywords:	Seismic noise < SEISMOLOGY, Seismic interferometry < SEISMOLOGY, Wave scattering and diffraction < SEISMOLOGY

Directionality of Ambient Noise in the Mississippi Embayment

By

Chunyu Liu

Khurram Aslam

and

Charles A. Langston

Center for Earthquake Research and Information
University of Memphis

Submitted to GJI, seismology

cliu5@memphis.edu

901-319-9233

Submission date: October 23rd, 2019

Summary

Cross-correlations of ambient seismic noise from 277 broadband stations within the Mississippi embayment (ME) with at least 1-month of recording time between 1990 and 2018 are used to estimate source locations of primary and secondary microseisms. We investigate source locations by analyzing the azimuthal distribution of the signal-to-noise ratio (SNR) and positive/negative amplitude differences. We use 84 stations with continuous 1-year recordings to explore seasonal variations of SNRs and amplitude differences. We also investigate the seasonal ambient noise ground motions using 2D frequency-wavenumber analysis of a 50-station array composed of the Northern Embayment Lithosphere Experiment. We observe that (1) two major azimuths can be identified in the azimuthal distribution of SNRs and amplitude difference. We also observe two minor azimuths in the seasonal variation of SNRs, amplitude difference, and 2D FK power spectra. Monthly 2D FK power spectra reveal that two energy sources are active in northern hemisphere winter and two relatively weak sources are active in summer. (2) Back-projection suggests that primary microseisms originate along the coasts of Australia or New Zealand, Canada and Alaska, Newfoundland or Greenland, and South America. (3) Secondary microseisms are generated in the deep water of the northern and southern Pacific Ocean, along the coasts of Canada and Alaska associated with near-shore reflections, and in the deep water of south of Greenland. (4) The azimuthal distribution of amplitude difference of sedimentary Love waves in the period band of 1-5s indicates a local source related to the basin-edge of the ME.

Key words: Ambient noise; Directionality; 2D FK beamforming.

1 Introduction

Ambient seismic noise in the short period band (1-20 s) is termed “microseisms”. Seismic noise with periods less than 5 s may be associated with anthropogenic activities (Lin et al. 2013; Nakata et al. 2015) or induced by basin-edges (Rovelli et al. 2001; Joyner 2000). Noise with periods between 5s and 20s is generated by different natural mechanisms (Wiechert 1904; Hasselmann 1963; Longuet-Higgins 1950). Primary (10-20s) and secondary (5-10s) microseisms are the two dominant types of noise in this band (Kibblewhite & Ewans 1985; Kedar et al. 2008). Primary microseisms are related to direct interaction of ocean swells with the ocean floor near coasts (Hasselmann 1963) with the secondary microseisms being associated with the interaction between two primary ocean waves with the same frequency ranges but different propagation directions (Longuet-Higgins 1950). Numerical modeling of the generation of secondary microseisms suggests that the interaction can be in deep or shallow water (Ardhuin et al. 2011). In deep water, the interaction can be between wind-driven waves with a broad directional spectrum or two independent wave systems. In shallow water, the interaction can be between coastal reflections and the primary ocean wavefield (Ardhuin et al. 2011).

Under the assumption of uniformly distributed seismic noise sources, cross-correlation (CC) of continuous ambient noise recorded at two stations can effectively retrieve a Green's function between them (Weaver & Lobkis 2001; Snieder 2004; Wapenaar 2004; Derode et al. 2003). In the past decade, tomography using ambient noise CCs has been applied globally (Ritzwoller et al. 2002; Nishida et al. 2009), regionally (Lin et al. 2008; Liang & Langston 2008; Liang & Langston 2009; Lin et al. 2007; Fu & Li 2015; Yao et al. 2006), and locally (Lin et al. 2013). Ambient noise tomography provides additional constraints on velocity structure for regions of active seismicity and sheds light on possible anomalous velocity structure for regions without local seismic sources.

96 Ambient noise CCs can also be applied to monitor time-varying processes. Long-term monitoring of phase or arrival time differences of scattered waves in ambient noise CCs provides an opportunity to estimate possible seismic velocity changes in the crust. Estimating crustal velocity changes further advance our understanding of volcanic eruptions (Brenguier et al. 2008b; Duputel et al. 2009), fault zone coseismic damage and postseismic healing (Brenguier et al. 2008a; Wu et al. 2016; Liu et al. 2018b), crustal response to external loads such as precipitation (Sens-Schönfelder & Wegler 2006), temperature (Meier et al. 2010; Hillers et al. 2015) and atmospheric pressure (Niu et al. 2008; Silver et al. 2007).

Although ambient noise tomography provides an additional pathway for understanding Earth structure, it suffers from accuracy problems because noise sources are usually heterogeneously distributed across the globe (Yang & Ritzwoller 2008; Stehly et al. 2006; Behr et al. 2013; Tian & Ritzwoller 2015). In the northern hemisphere, sources are distributed in the northern Pacific and Atlantic, and the energy of sources varies seasonally from high energy in the winter to low in the summer (Young 1999). In the southern hemisphere, swells from storms penetrate throughout the Indian, Pacific, and Atlantic Oceans; the energy of sources is high in northern hemisphere summer and low in winter. The reason why ambient noise CCs can retrieve the Green's function is still unclear. Recent studies have revealed that uneven noise source distributions can influence the accuracy of velocity and azimuthal anisotropy tomographies (Tsai 2009; Weaver et al. 2009; Yao & Van Der Hilst 2009; Harmon et al. 2010). Thus, better knowledge of noise source distributions can help to assess the uncertainty of velocity tomography as well as understanding the mechanisms for noise generation.

As seen from North America, microseisms can originate from different locations and be related to different generation mechanisms. Source locations are rather complicated for the western

United States. For the secondary microseisms, seasonal variability of noise is weak and strong noise arrives from southwest quadrant, from the California coasts or from the deep Pacific Ocean (Tian & Ritzwoller 2015; Yang & Ritzwoller 2008). Strong seasonal variability can be observed for primary microseisms. In northern hemisphere winter, the strongest signals arrive from northwest and northeast quadrants, probably from the northern Pacific and Atlantic coasts of North America (Gerstoft et al. 2008; Landès et al. 2010; Kedar et al. 2008; Retailleau et al. 2017; Stehly et al. 2006) or near the southern tip of Greenland (Kedar et al. 2008). In northern summer, strong signals arrive from the south and southwest quadrants, from the California coasts (Tian & Ritzwoller 2015; Yang & Ritzwoller 2008). Source locations for primary and secondary microseisms in eastern United States have been seen to have no significant differences. For primary and secondary microseisms, strong noise arrives from the northeast and west, from the coast of Newfoundland (Cessaro 1994; Langston et al. 2009) or Pacific coast of North America (Yang & Ritzwoller 2008). Microseisms can also be related to localized sources including rivers (Burtin et al. 2008), and lakes (Gu & Shen 2012).

A variety of methods have been used to infer source locations of the ambient noise. Shapiro et al. (2006) located sources for 26s microseisms off the west African coast in the Gulf of Guinea by minimizing the travel time misfit using a grid search method. Grid searching over the maximum stacked energy (Gu et al. 2007; Zeng & Ni 2010) has also been applied to locate sources. Tian & Ritzwoller (2015) and Yang & Ritzwoller (2008) identified different source locations for primary and secondary microseisms by a statistical analysis of the azimuthal distribution of the signal-to-noise ratio (SNR). Behr et al. (2013) used three-component plane wave beamforming to infer source locations for primary and secondary microseisms in New Zealand and suggested different back-azimuths for primary Rayleigh and Love waves but similar ones for secondary Rayleigh and Love waves.

Studies of ambient noise source locations in the Mississippi embayment (ME) are quite limited (Yang & Ritzwoller 2008; Langston et al. 2009) but important for the following reasons. Firstly, the ME is a SSW plunging trough filled with up to 1.5 km of unconsolidated sediments (Fig. 1) (Hildenbrand & Hendricks 1995), and hosts one of the most active seismic zones in the North America, the New Madrid seismic zone (NMSZ). Better knowledge of the noise source locations can help to assess the accuracy of previous tomography studies (Liang & Langston 2008, 2009; Chen et al. 2016; Liu et al. 2018a), which can improve confidence on determining earthquake parameters within the NMSZ. Secondly, recent broadband deployments of the EarthScope Transportable Array (TA) and Northern Embayment Lithosphere Experiment (NELE) within the ME provide an opportunity to apply location methods for an array with an excellent azimuthal distribution of stations. Lastly, the ME sediment variation can also be a potential source for generating sedimentary surface waves (Langston et al. 2005, 2009; Liu et al. 2018a). Observations of source locations of sedimentary surface waves can help the understanding of the generation mechanisms and how the sediments influence wave propagation.

In this study, we investigate the azimuthal distribution of sources for primary and secondary microseisms, explore the seasonal variation of ambient noise sources by monitoring the changes of the SNRs, amplitude differences, and 2D FK power spectra, and search for local sources in the embayment using low-period ambient noise ($T < 5$s).

2 Data and methods

We use data from 277 broadband stations (Fig. 1) installed between 1990 and 2018 to compute vertical-vertical (ZZ) and horizontal-horizontal (TT) component CCs. The interstation distances are chosen to be larger than three times the microseism wavelength and data must be time-contiguous for at least 30 days. These data have been used to image lithospheric shear wave velocity structure by Liu et al. (2018a). We use the MSNoise python package (Lecocq et al. 2014) to compute the CCs. The preprocessing procedures can be summarized as follow: 1) broadband miniseed data are requested from IRIS through the FDSN service, 2) removing the instrument response, 3) bandpassing from 0.05 to 1 Hz, 3) removing transients and earthquake signals using temporal normalization as described by Bensen et al. (2007), and 4) partially eliminating the effect of heterogeneous distributed noise sources on the CCs by spectral whitening.

We apply statistical analyses of SNRs and positive/negative amplitude differences as well as 2D frequency-wavenumber (FK) analysis of the instrument-corrected data to constrain the back-azimuths of strong noise sources. The processing procedures in each method are described in the following sections.

Energy flux directions of microseisms can be identified from the azimuthal distribution of SNRs (Tian & Ritzwoller 2015; Yang & Ritzwoller 2008). The SNR is defined to be the ratio between the maximum absolute amplitude of crustal surface wave arrivals (~ 3 km/s) and the root-mean-squared (RMS) amplitude of noise in the coda window. In the primary (10-20s) or secondary (5-10s) microseisms passband, we define the coda window as the last 200s of CCs where no direct surface wave arrivals are observed (Fig. 2). Yang & Ritzwoller (2008) suggested that the RMS amplitude of noise after the major crustal surface wave arrival is similar for the CCs within the same seismic array. Fig. 3(A) shows CCs between the virtual source at HENM station and all

186 surrounding stations. The positive lag portion of the CCs is the outgoing wave from the virtual 187 source. For a CC between the virtual source A and station B, the outgoing wave from the station 188 A is the incoming wave for the station B. Thus, we only use positive lags of CCs to compute the 189 SNR. We then correct SNR measurements for geometric spreading through: $\mathrm{SN}R_{corrected} = \mathrm{SNR} *$ 190 $\sqrt{D/_{300}}$, in which D is the interstation distance in km. Because SNR increases as the square root 191 of number of days to be stacked (Tian & Ritzwoller 2015), we only use stacks with 30 days of 192 data. All corrected SNR measurements for all CCs related to the virtual source A, with different 193 azimuths, are used to construct a rose diagram (Fig. 3(B)). The azimuths (Fig. 3(C)) here are from 194 the virtual source A to surrounding stations. The bars point to the wave propagation direction for 195 sources of microseisms (away-from-the-source). If noise sources are distributed homogeneously 196 in azimuth, then each SNR value should have the same length. If there is a dominant source 197 direction, then bars will get relatively longer in the direction away from the source.

198 We also use the amplitude difference of crustal surface waves seen at positive and negative 199 lags of the CCs to estimate the strength of noise. The amplitude difference is defined as: $\mathrm{Am}p_{diff}$ 200 $= (Amp_{pos} - Amp_{neg}) * 10000$, in which $\mathrm{Am}p_{pos}$ and $\mathrm{Am}p_{neg}$ are the maximum amplitude of 201 crustal surface waves on positive and negative lags of the CCs, respectively. The amplitude 202 difference is exaggerated 10000 times for better comparison with the SNR measurements. The 203 amplitude difference is also corrected for the geometric spreading. If the corrected amplitude 204 difference is larger than 200, we set the value to be 200. For a CC between the virtual source A 205 and the receiver B, if the amplitude of the crustal surface wave on the positive lag is larger than 206 that on the negative lag, the back-azimuth from the receiver B (Fig. 3(C)) can indicate the direction 207 of the source. Otherwise, we use azimuth. A collection of amplitude difference measurements for

all CCs related to the virtual source A is used to construct a rose diagram in which large amplitude difference indicates the source direction (toward-the-source).

We verify the source directions determined from the azimuthal distribution of SNRs and amplitude differences through 2D FK analysis of a subset of stations used as a phased array (Langston et al. 2009; Behr et al. 2013; Aki & Richards 1980; Capon et al. 1973). The reference station in the 2D FK analysis of primary microseisms is the center of an array composed of 50 stations deployed in 2014 as part of the Northern Embayment Lithosphere Experiment (Fig. 4). The location of the center is defined by averaging latitude and longitude of array station locations. In addition to inferring wave direction and slowness, we also compute the monthly 2D FK power spectra to investigate seasonal variations in the noise. This is done by: cutting the time-series into 24 hourly segments; computing 2D FK power spectra for each one-hour segment; and then stacking hourly 2D power spectra into monthly power spectra. To clearly estimate the wave directions, we compute the 2D FK power for different days. The power spectra are binned with slowness between 0.27 s/km to 0.35 s/km and a 2° azimuth interval. In each bin, we remove mean to better observe power difference in different azimuth for different days and use maximum value to represent the power.

Investigating seasonal variations of SNRs and amplitude differences can also help reveal back-azimuths of noise sources. The hypothesis that microseisms originate from arrivals of strong storms has been confirmed by Stehly et al. (2006). Strong storms appear in the northern Pacific and Atlantic during northern hemisphere winter and the southern Indian and Pacific Oceans during northern hemisphere summer (Young 1999; Stehly et al. 2006). We use the vertical component of 84 broadband stations (Fig. 1) with continuous recording to compute the CCs over the months of 2014. For each month, SNRs and amplitude differences are computed from all CCs. Because the directional output from SNR and amplitude difference measurements are different, away-from-the-source in SNR and toward-the-source for amplitude difference measurements, we convert away-from-the-source to toward-the-source for better comparison. We then bin SNRs and amplitude difference measurements into 5° back azimuth intervals. The RMS of SNRs and amplitude differences are computed. Collections of azimuthal variations of SNRs or amplitude difference in different seasons can provide direct observations of major source back-azimuths.

A simple back-projection along the great circle from the network location can provide an idea of source locations. The back-projection needs two major parameters, the location of the array and the back-projection direction. We use the center of array ($-90°, 35°$) as our reference location and means $\pm$ standard deviations as our back-projection directions. We use a nonlinear regression fitting function in Matlab, fitnlm (DuMouchel et al. 1989; Holland et al. 1977; Seber et al. 2003), to compute the means and standard deviations. The fitting function has the form of: $y = a + c1 * \mathrm{e}^{-(x-c2)^2}/c3 + d1 * \mathrm{e}^{-(x-d2)^2}/d3 + m1 * \mathrm{e}^{-(x-m2)^2}/m3 + n1 * \mathrm{e}^{-(x-n2)^2}/n3$, in which a, $c1$, $c1$, $c2$, $c3$, $d1$, $d2$, $d3$, $m1$, $m2$, $m3$, $n1$, $n2$, and $n3$ are unknown.

3 Results

3.1 Azimuthal distribution of SNRs and amplitude differences

In the following, "Rayleigh primary" and "Rayleigh secondary" correspond to the ZZ correlation Green's functions for primary and secondary microseisms, respectively. Likewise, "Love primary" and "Love secondary" correspond to the same microseisms for the TT correlation Green's functions. We compute 13,445 and 11,977 ZZ and TT component CCs, respectively. For each CC, we compute the SNRs and amplitude difference. To investigate the azimuthal bias of station pairs on the measurements of SNRs and amplitude difference, we compare the azimuthal distribution of station pairs with SNRs/amplitude difference measurements for four networks: Central and Eastern US network (N4), Cooperative New Madrid Seismic network (NM), USArray Transportable Array (TA), and Northern Embayment Lithospheric Experiment (ZL). Very good azimuthal coverage (Top left corner inserted map) for the four networks can be observed in Fig. 5 and Fig. 6. Two major away-from-the-source and toward-the-source directions can be identified in azimuthal distribution of SNRs (Fig. 5) and amplitude difference (Fig. 6), respectively. We observe no significant difference on two directions in the rose diagram of Rayleigh (or Love) primary and secondary microseisms.

3.2 2D Frequency-wavenumber analysis

The slowness and back-azimuth are well resolved provided signals correlate across this large regional array (Fig. 4). In Fig. 7, we stack hourly 2D FK power spectra to construct monthly power spectra for Rayleigh primary microseisms. A homogenous source distribution can be observed as the circular feature in the spectral plots, but the magnitude of the energy flux has clear azimuthal maxima. Energy flux with back-azimuths of $\sim\mathbf{40}°$ and $\sim\mathbf{320}°$ emerge for the whole year but the energy is stronger in winter than summer. Energy flux with back-azimuths of $\sim\mathbf{120}°$ and $\sim\mathbf{260}°$ become visible from March to September. In Fig. 8, the noise sources are heterogeneously distributed. Major energy flux emerges in northeast and northwest quadrants. Weak energy flux can be observed in southwest and southeast quadrants in April/May and June, respectively. To estimate the exact azimuths of energy flux from 2D FK power spectra, we investigate seasonal variation of normalized power with the azimuths (Fig. 9). Four major back-azimuths can be identified. We observe a small difference, $\sim\mathbf{255}°$ for Rayleigh primary and $\sim\mathbf{270}°$ for Rayleigh secondary, on the back-azimuths of noise energy flux in the southwest quadrant.

3.3 Seasonal variability of SNRs and amplitude difference

We also compute 1670 vertical component CCs to investigate seasonal variations of azimuthal distribution of SNRs and amplitude difference. In Fig. 10, different color lines represent average SNRs and amplitude differences for different months in 2014. Four major back-azimuths, $\sim\mathbf{40}°$, $\sim\mathbf{140}°$, $\sim\mathbf{260}°$ and $\sim\mathbf{320}°$, are identified in the azimuthal distribution of the SNR and amplitude difference. A small difference, $\sim\mathbf{255}°$ for Rayleigh primary and $\sim\mathbf{270}°$ for Rayleigh secondary, can also be observed. For noise with back-azimuths of $\sim\mathbf{140}°$ and $\sim\mathbf{260}°$, average SNRs and amplitude difference from July to September are higher than those from November to March. For noise with back-azimuths of $\sim\mathbf{40}°$ and $\sim\mathbf{320}°$, average SNRs and amplitude difference from November to March are higher than those from May to July.

3.4 Directionality of sediment surface wave

We compute 1247 TT and 989 ZZ component CCs for station pairs with interstation distance less than 100 km in the passband of 1-5 s. We observe 390 and 86 CCs with low-velocity sedimentary Love waves (group velocity of ~ 450 m/s) and Rayleigh waves (group velocity of ~ 750 m/s), respectively (Fig. 11). We construct a rose diagram of amplitude difference for sedimentary Love waves and do not observe obvious maximums in the third quadrant (Fig. 11(C)).

4 Discussion

4.1 Source locations for primary and secondary microseisms

We fit four joint Gaussian functions to the azimuthal distribution of SNRs to estimate the means and standard deviations (Fig. 12). In Table 1, the back-projection direction measured from different methods are comparable to each other for primary and secondary microseisms. A simple back-projection (Fig. 13) using the Gaussian mean and standard deviation provides insight on the source locations.

The noise with the back-azimuth of $\sim\mathbf{45°}$ has the strongest energy. Back-projection from the center of the network shows that the source locations for primary and secondary microseisms are in the northern Atlantic Ocean or along North America coasts. The strongest energy source in the northern hemisphere during winter appears in the Atlantic Ocean (Stehly et al. 2006; Ardhuin et al. 2011). Kedar et al. (2008) suggested that sources of secondary microseisms for this strong energy are in the deep water of south of Greenland. Retailleau et al. (2017) proposed that sources for primary microseisms are along the coast of Greenland. Similar source locations for body waves at 0.1-0.3 Hz have also been observed through beamforming analysis by Landès et al. (2010). Langston et al. (2009) suggested that source locations for microseisms in the 4-5 s period passband can be along the coast of Newfoundland in northeastern North America through wave gradiometry and frequency-wavenumber analysis. A wide-angle triangulation (Cessaro 1994) also suggested the sources for primary microseisms are along the coasts of Newfoundland. Since previous studies (Bromirski & Duennebier 2002; Cessaro 1994) infer shallow sources for primary microseisms, we suggest that sources for Rayleigh and Love primary microseisms are near the coasts of Newfoundland or Greenland. The source of secondary microseisms can be 1) off the coast of Newfoundland and be related to the interaction between ocean swell with coastal reflection, or 2) in the deep water of south of Greenland.

For noise with the back-azimuth of $\sim\mathbf{125°}$ measured from the receivers, the noise energy flux is stronger in summer than winter, which suggests that sources can be in the southern hemisphere. Back-projections along great circles suggest noise sources for primary microseisms can be near the coasts of South America. Ardhuin et al. (2011) observed no significant seismic noise from reflection near the coasts of South America, so the source for secondary microseisms can be in the southern Atlantic Ocean.

For noise with the back-azimuth of $\boldsymbol{\sim 260^\circ}$ from the receivers, previous studies proposed that the sources might be in the southern Pacific Ocean and near the coastal region of Australia or New Zealand. Tian & Ritzwoller (2015) suggested that the sources for primary microseisms with the back-azimuth of ~220° can be in the Pacific Ocean of the southern hemisphere. Stehly et al. (2006) also observed that sources for Rayleigh primary microseisms can be generated in the southern Pacific Ocean and near the southern and eastern coastal regions of Australia and New Zealand in southern Indian Ocean during the northern hemisphere summer. Gerstoft et al. (2008) and Landès et al. (2010) observed possible source locations for body waves at 0.1 - 0.3 Hz in the southern Pacific. A slight difference on propagation directions (~255° for Rayleigh primary and ~ 270° for Rayleigh secondary in Fig. 9 and 10) may indicate that sources are in different regions. Primary microseisms (~ 255°) can be generated near southern coasts of Australia or northwest coasts of New Zealand (Reading et al. 2014; Stehly et al. 2006). Great circle back-projections indicate that secondary microseisms (~ 270°) can be in the deep Pacific Ocean of the southern hemisphere.

For noise with the back-azimuth of $\boldsymbol{\sim 320^\circ}$, many studies indicated sources can be near the coasts of Canada and Alaska or in the deep northern Pacific Ocean. Tian & Ritzwoller (2015) proposed that primary microseisms identified in the Juan de Fuca plate area are generated in the shallow water near the Graham island. Stehly et al. (2006) suggested primary microseisms might be generated from two low energy sources, one near the coast of Alaska and the other close to Japan. Gerstoft et al. (2008) and Landès et al. (2010) proposed sources for seismic body waves can be in the deep ocean of the Pacific. Ardhuin et al. (2011) revealed that coastal reflections can significantly increase the secondary microseisms along the western coast of Alaska and California. The primary microseisms can be generated near the coastlines of Alaska and Canada. Secondary microseisms can be originated near coasts and be related reflections or in the deep Pacific Ocean.

4.2 Directionality of the Sedimentary Surface Wave

Sedimentary surface waves can be used to image the sediment velocity structure and understand wave propagation properties (Lin et al. 2013; Langston et al. 2009). A complex interaction between body waves, diffracted waves and basin-edges might induce surface waves, called basin-induced surface waves (Nayaran 2012; Field 1996; Hatayama et al. 1995; Furumura & Sasatani 1996; Kawase 1996). Comparing the azimuthal distribution of the amplitude difference for sedimentary Love waves and the geometry of the basin, we suggest that the generation of the sediment Love wave might be related to the basin edge.

5 Conclusions

We investigate source locations of Rayleigh and Love primary/secondary microseisms through statistical analyses of SNRs and amplitude difference, and 2D frequency-wavenumber analysis. We use 277 broadband stations to construct 13,445 and 11,977 ZZ and TT component CCs. Two major directions can be identified in the azimuthal distribution of SNR and amplitude difference for primary and secondary microseisms. We also use 84 stations which continuously record in 2014 to estimate seasonal variations of seismic noise. Seasonal variations of SNRs and amplitude difference locate another two weak noise sources in the southern hemisphere. Additionally, we use 390 TT component CCs to investigate generation mechanisms of sedimentary surface waves. Comparing the azimuthal distribution of amplitude difference of sedimentary surface waves and

369 the geometry of the edge of the ME, we propose the generation of sedimentary Love waves might
370 be related to the basin-edge.

371 In the primary microseisms band, four major back-azimuths, 45°, 125°, 255° and 320°,
372 are identified. For noise with the back-azimuth of 255°, noise energy flux is stronger in northern
373 hemisphere summer than winter, which indicates that noise sources must be in the southern
374 hemisphere. A simple back-projection reveals that noise sources can be along the coast of Australia
375 or New Zealand. For noise with the back-azimuth of 320°, major noise sources could be along the
376 coasts of Canada and Alaska, which are consistent with regions identified by Tian & Ritzwoller
377 (2015) and Stehly et al. (2006). For noise with the back-azimuth of 45°, sources can be near the
378 coasts of Newfoundland or Greenland. For noise with the back-azimuth of 125°, strong energy
379 flux in northern hemisphere summer suggests that noise sources are located in the southern
380 hemisphere. A simple back-projection reveal that sources can be along southeast coasts of South
381 America.

382 In the secondary microseisms band, four major azimuths, 45°, 125°, 270° and 320°, are
383 observed. Sources for noise with the back-azimuth of 270° can be in the Pacific Ocean of the
384 southern hemisphere, where sources for body waves were suggested by Gerstoft et al. (2008) and
385 Landès et al. (2010). Sources for noise with the back-azimuth 320° can be near the coasts of
386 Alaska and Canada or can be in the deep Pacific Ocean (Gerstoft et al. 2008; Landès et al. 2010).
387 Due to low reflection energy near the coastlines of Newfoundland, sources for noise with the back-
388 azimuth 40° can be in the deep ocean of south of Greenland.

389 In the 1-5s period passband, low-velocity sedimentary Love waves are observed in 390 CCs.
390 The azimuthal distribution of amplitude difference might indicate that the generation of

sedimentary surface waves are related to the basin-edge. Comprehensive waveform modeling or ground motion simulation is needed to better understand the generation mechanisms of sedimentary surface waves.

Acknowledgements

We appreciate funding from Center for earthquake research and information (CERI), University of Memphis. All microseism noise data can be obtained from the IRIS Data Management Center through FDSN service.

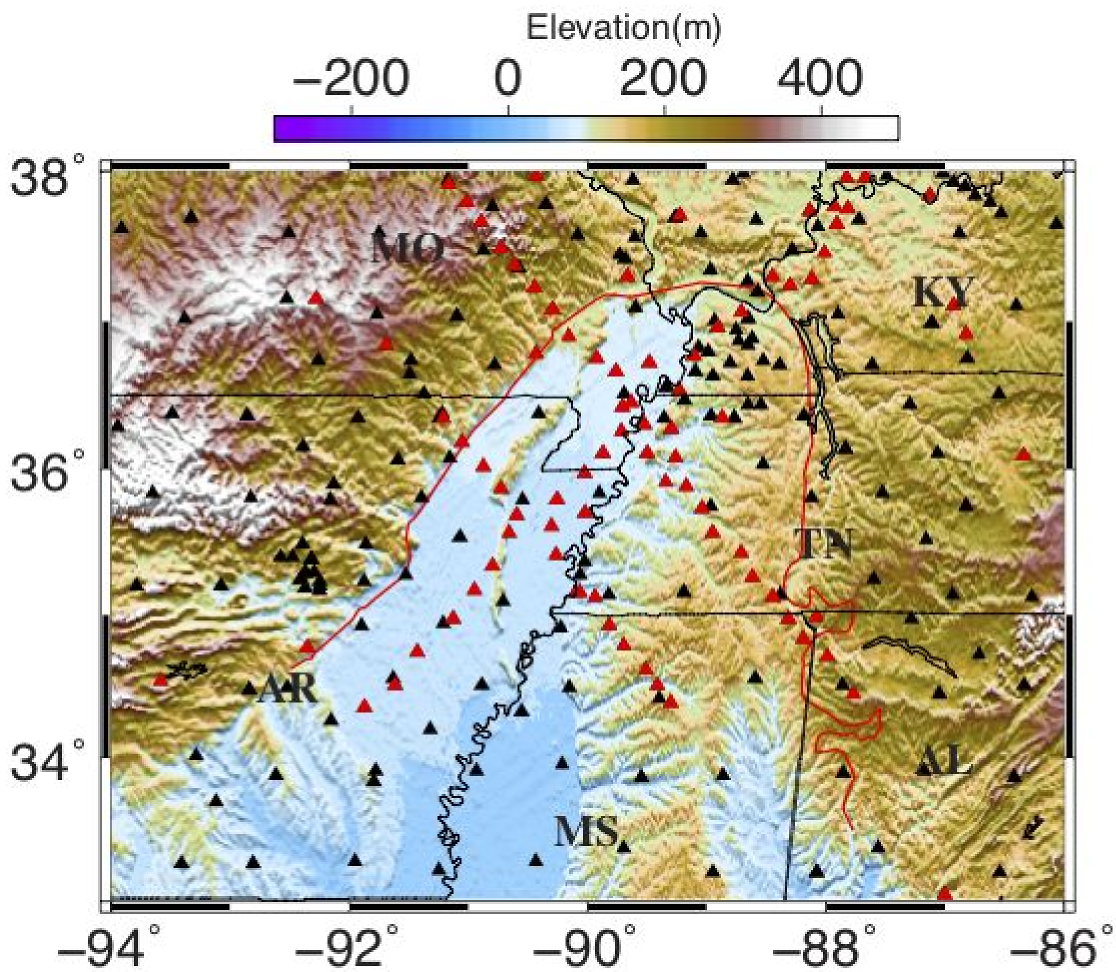

Figure 1. Index map of the Mississippi embayment in the central United States showing 277 broadband stations (triangles) installed in the period of 1990 to present, the sediment boundary (a red solid line) modified from Dart (1992) and Dart & Swolfs (1998), and bedrock topography (Amante & Eakins 2009). 84 Broadband stations marked with red triangles have continuous recording in 2014 and are used for the investigation of seasonal variations of SNR and amplitude difference. An additional 193 broadband stations marked with black triangles are used for construction of rose diagrams of SNR and amplitude difference.

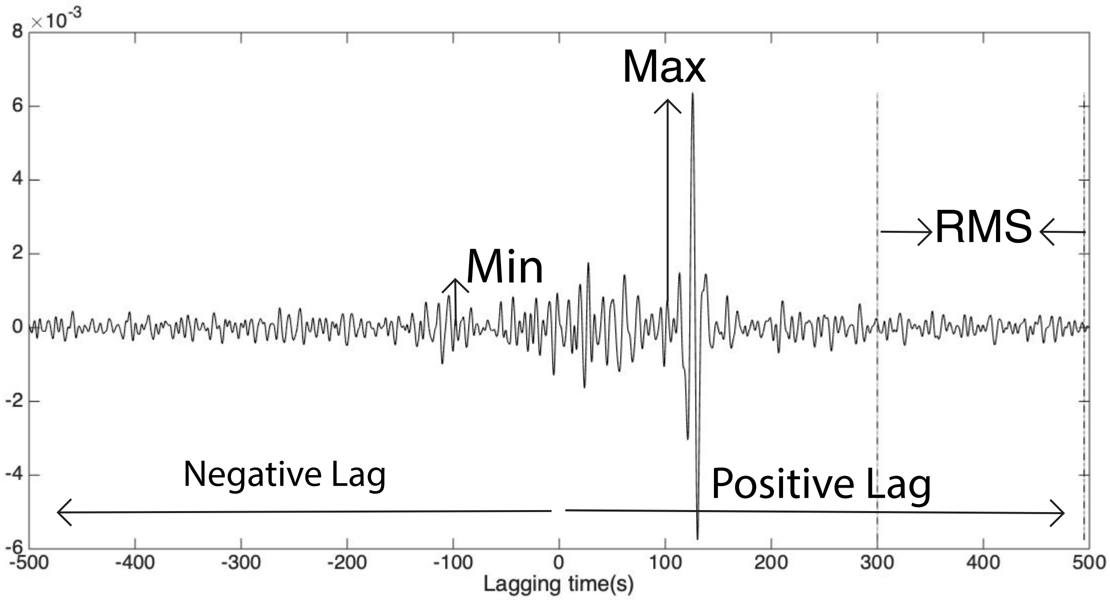

Figure 2. Illustration of the measurements of Signal-to-Noise Ratio (SNR) and amplitude difference. The ZZ cross-correlation is between PENM of the New Madrid Cooperative Seismic Network and Z48A of EarthScope's Transportable array in the passband of 0.05-0.2 Hz. The peak amplitude is the maximum of the absolute velocity for positive time lags. The RMS is the root-mean-square value of the velocity marked between two dashed lines. Amplitude difference is the difference of maximum amplitude in positive and negative lags and is exaggerated 10000 times for comparison with SNR measurements.

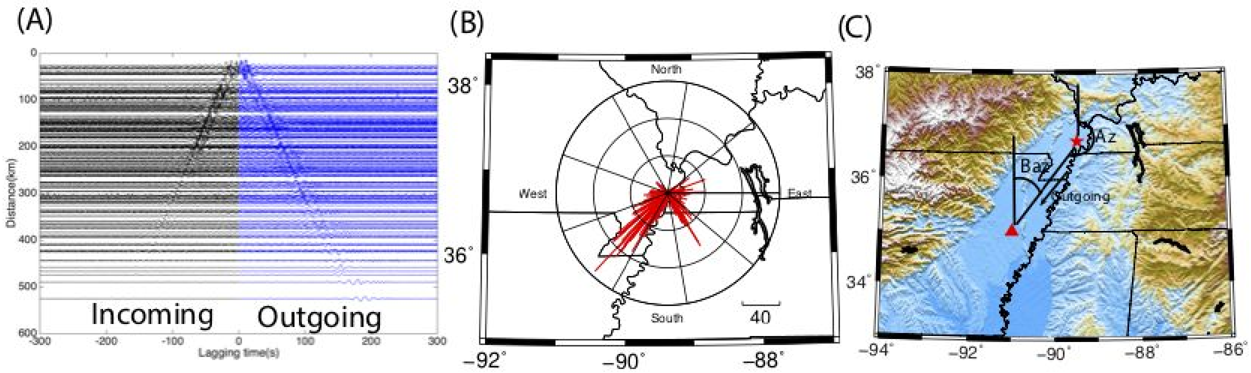

Figure 3. Construction of rose diagram of SNR. (A) CCs are between the virtual source HENM and all surrounding stations. Positive lags of CCs stand for outgoing wave propagation from the virtual source. (B) Each bar represents one SNR measurement on an outgoing wave between two stations. The length of the bar indicates the magnitude of the SNR measurements. Collection of SNR measurements, with different azimuths, constructs the rose diagram with a scale of 40 for each contour. (C) Azimuth and back-azimuth definition for rose diagrams.

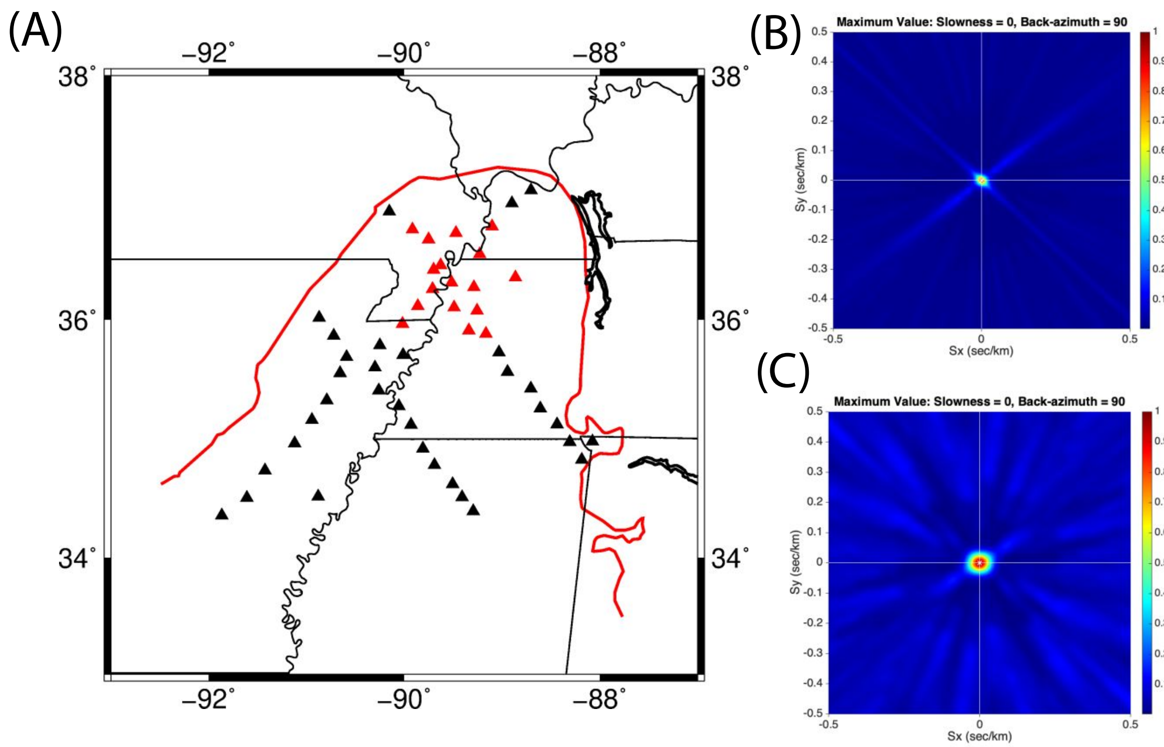

Figure 4. Array geometry (A) and array response functions (BC) for an incident plane wave. 17 stations marked with red triangles are used for 2D FK analysis of secondary microseisms (C). With additional 34 stations marked with black triangles, an array with 50 stations are used for 2D FK analysis of primary microseisms (B). Note the streaky side lobes (B) due to the dominance of the linear portions of the array composed of 50 stations.

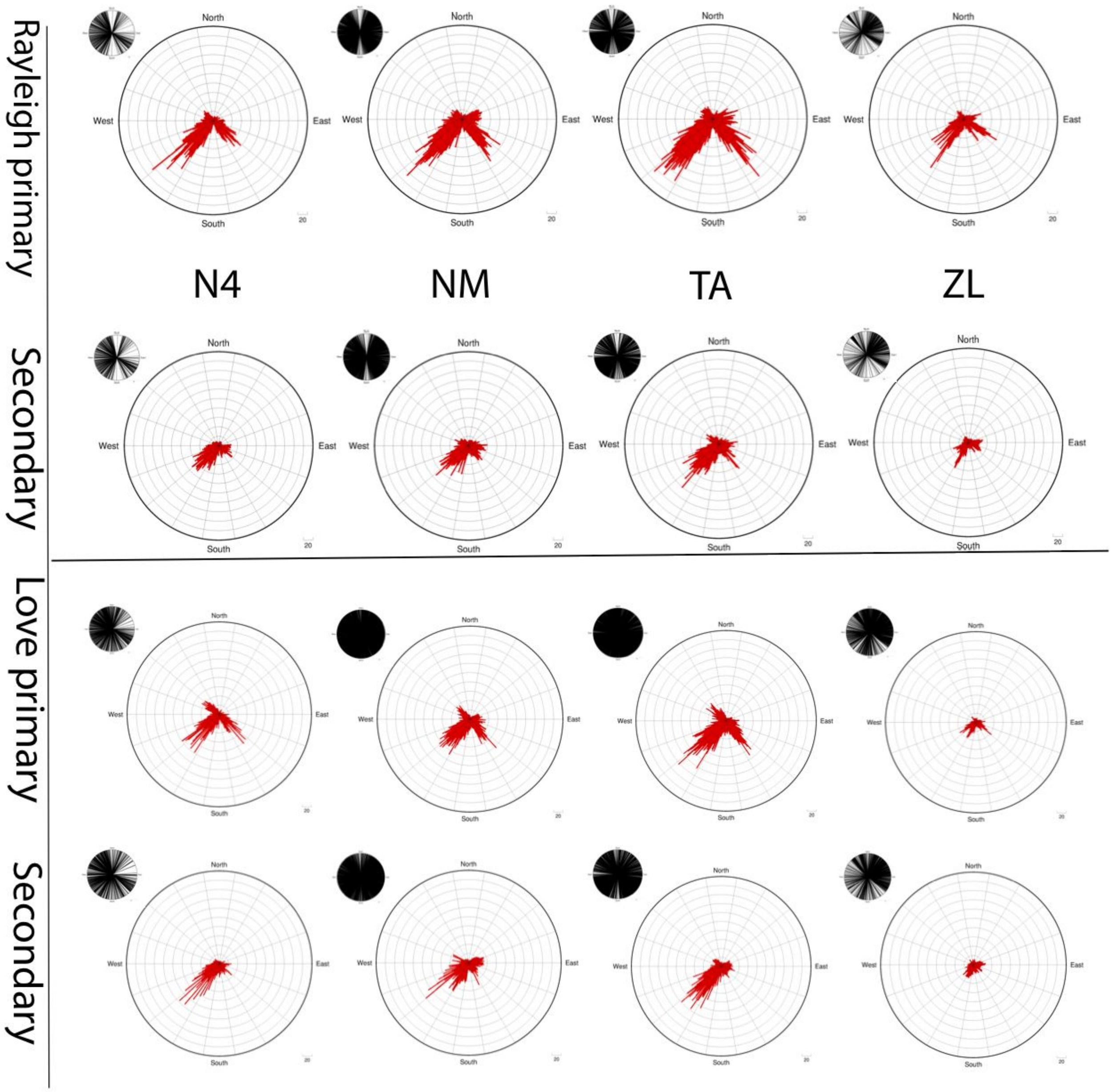

Figure 5. Rose diagrams of SNRs for four networks, N4, NM, TA and ZL. Inserted rose diagrams at the left corner show the azimuthal distribution of station pairs. Two major away-from-the-source directions can be identified in the southwest and southeast quadrants.

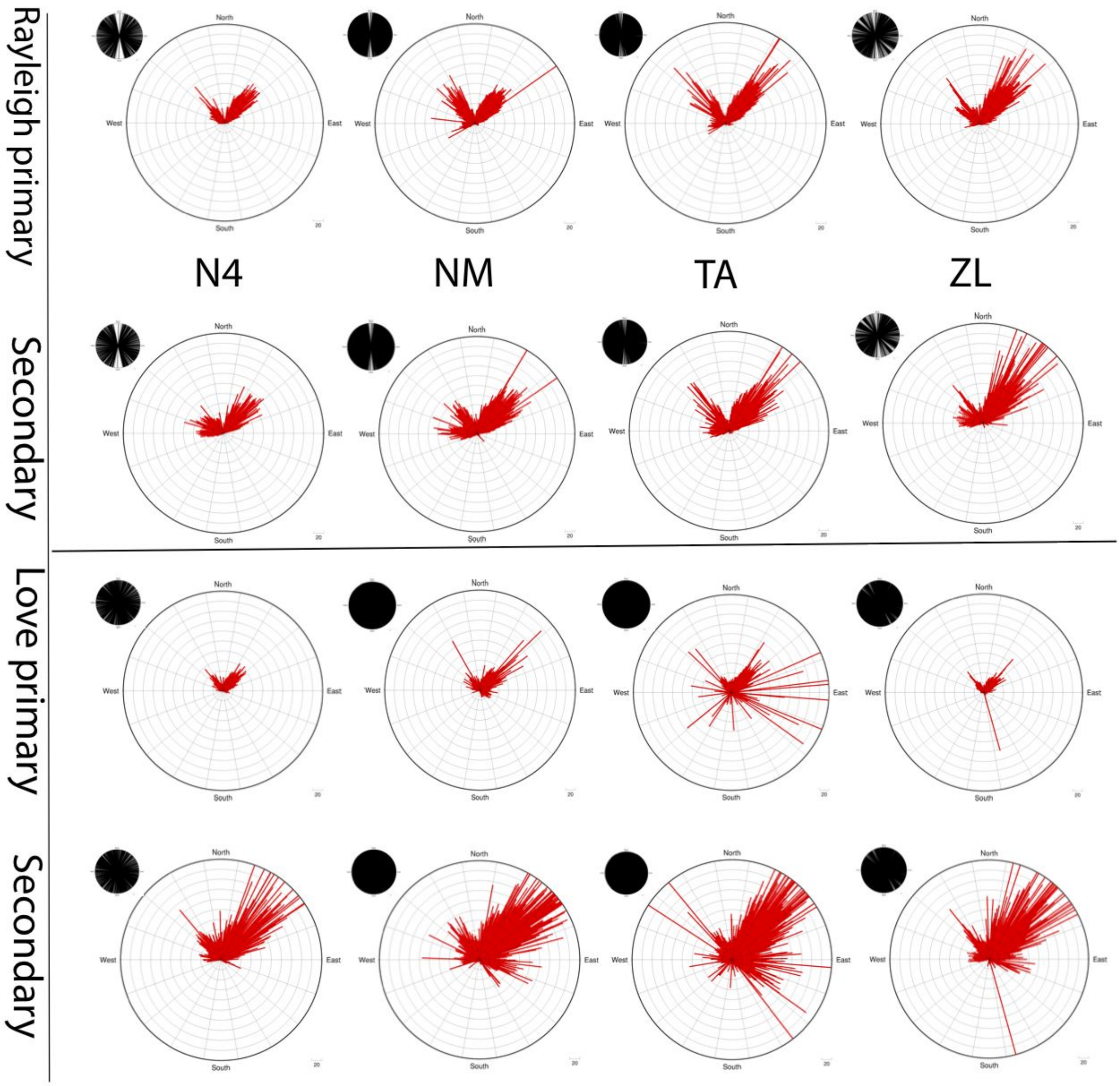

Figure 6. Rose diagrams of amplitude difference for four networks, N4, NM, TA, and ZL. Two major toward-the-source directions, in northeast and northwest quadrants, can be observed.

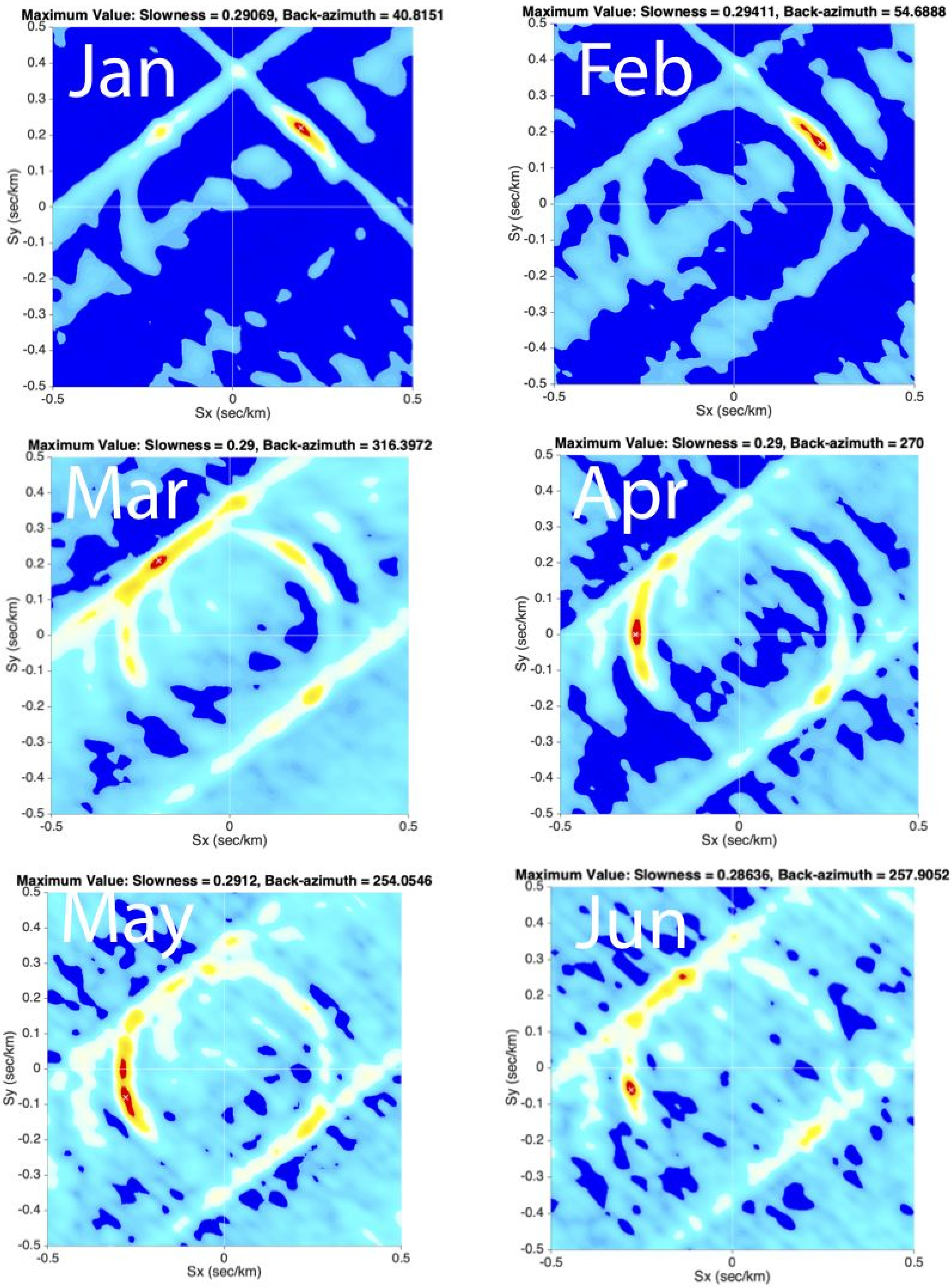
Maximum Value: Slowness = 0.29069, Back-azimuth = 40.8151
Jan
Maximum Value: Slowness = 0.29411, Back-azimuth = 54.6888
Feb
Maximum Value: Slowness = 0.29, Back-azimuth = 316.3972
Mar
Maximum Value: Slowness = 0.29, Back-azimuth = 270
Apr
Maximum Value: Slowness = 0.2912, Back-azimuth = 254.0546
May
Maximum Value: Slowness = 0.28636, Back-azimuth = 257.9052
Jun
Sy (sec/km)
Sx (sec/km)

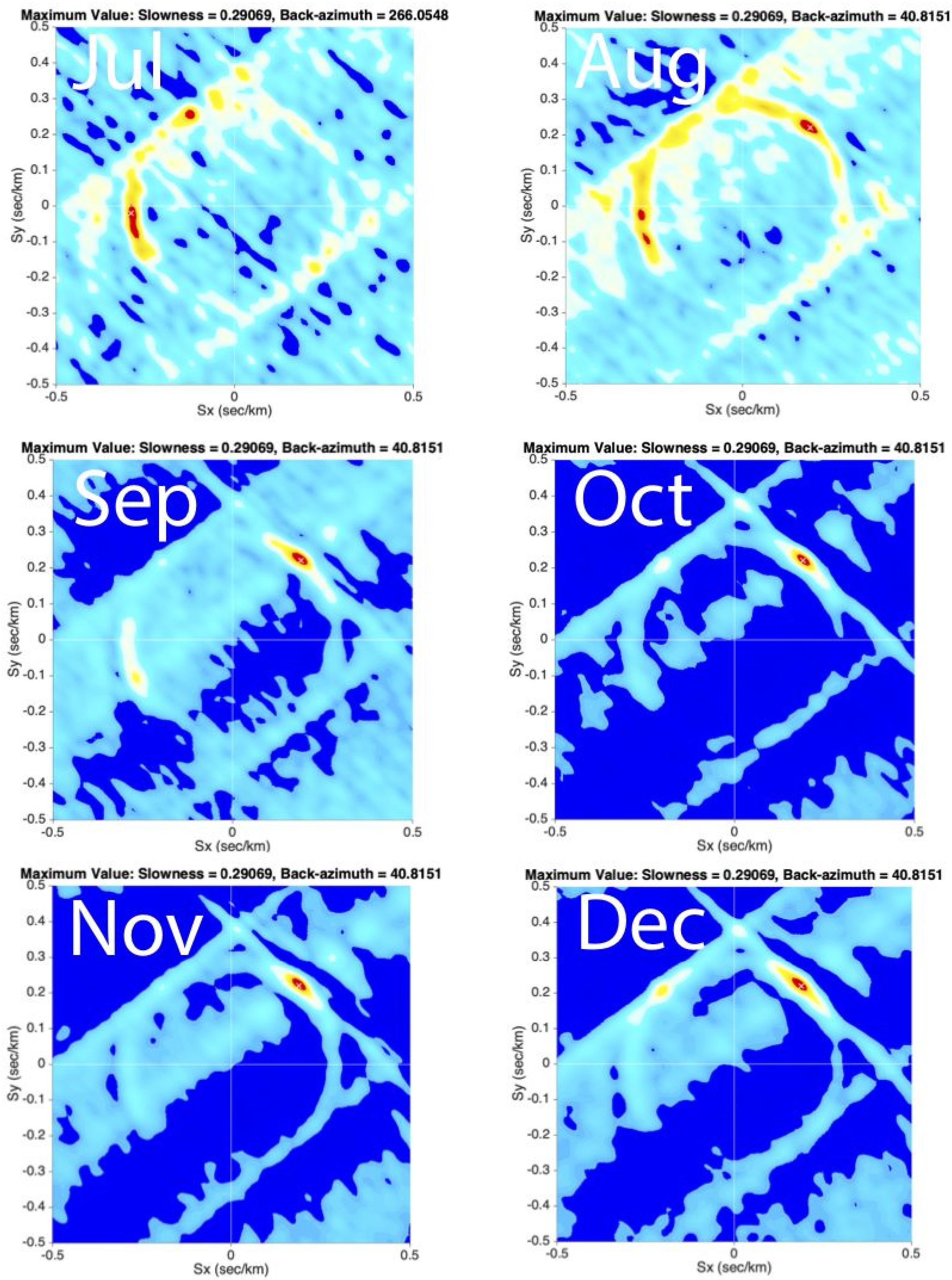

Figure 7. Monthly power spectra for Rayleigh primary microseisms in 2014. Energy flux with back-azimuths of ~40° and ~320° emerge during the whole year but the

energy is stronger in winter than summer. Energy flux with back-azimuths of ~120° and ~260° become visible from March to September.

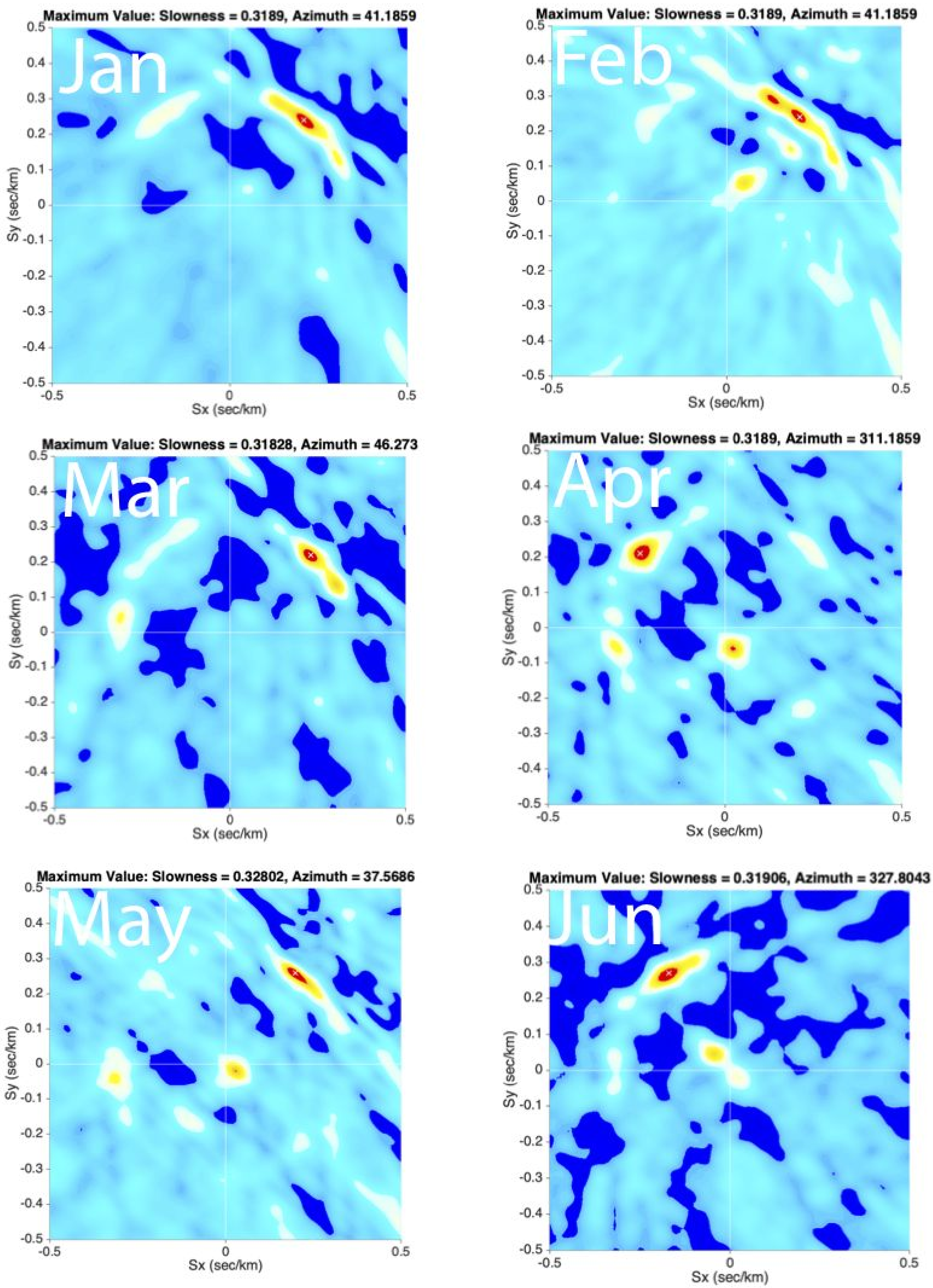

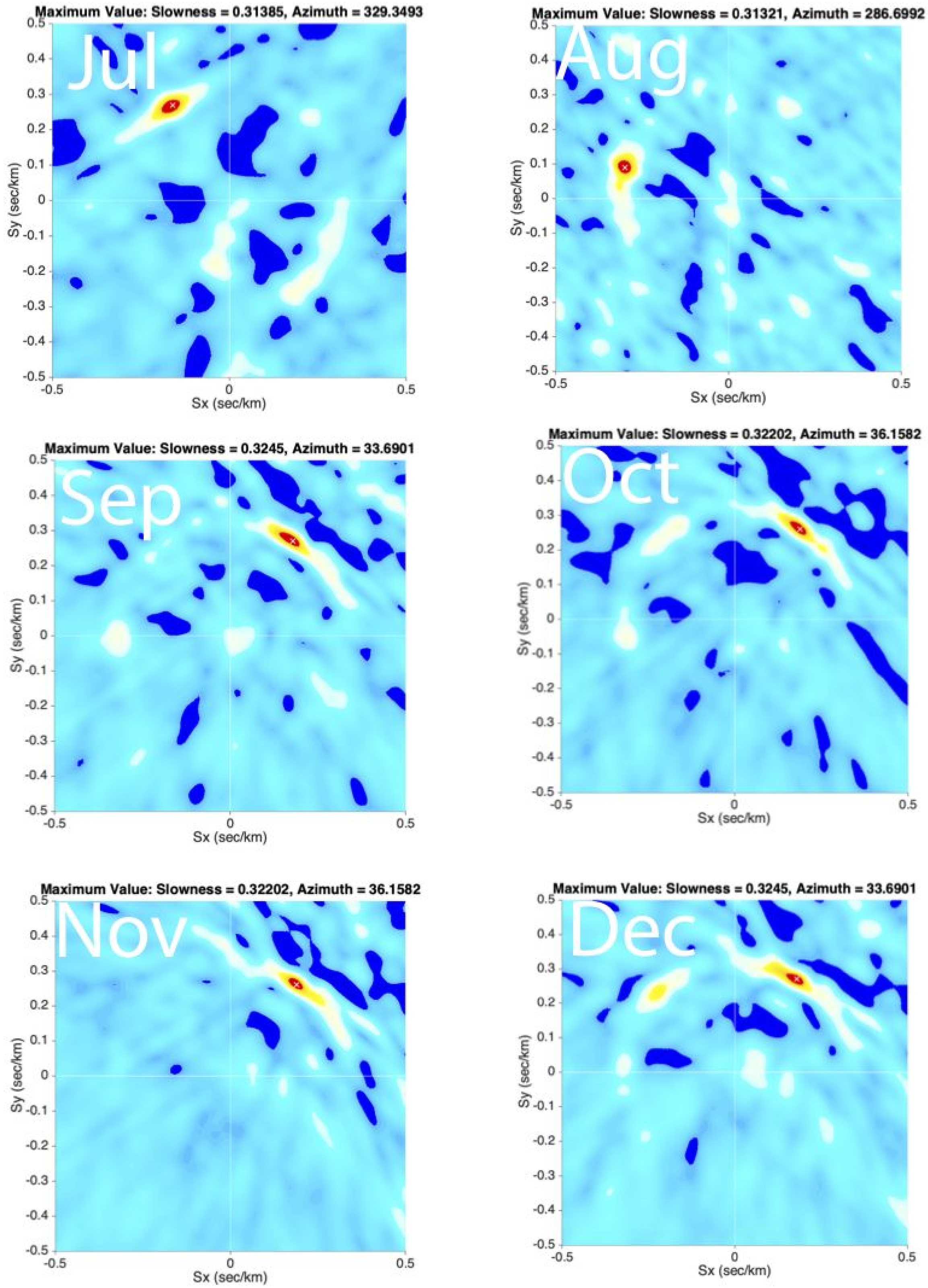

Figure 8. Monthly power spectra for Rayleigh secondary in 2014. Two strong energy fluxes with the back-azimuths of ~40° and ~320° emerge in northeast and northwest quadrants for the whole

year. Two additional energy fluxes emerge in the southeast and southwest quadrants from April to July.

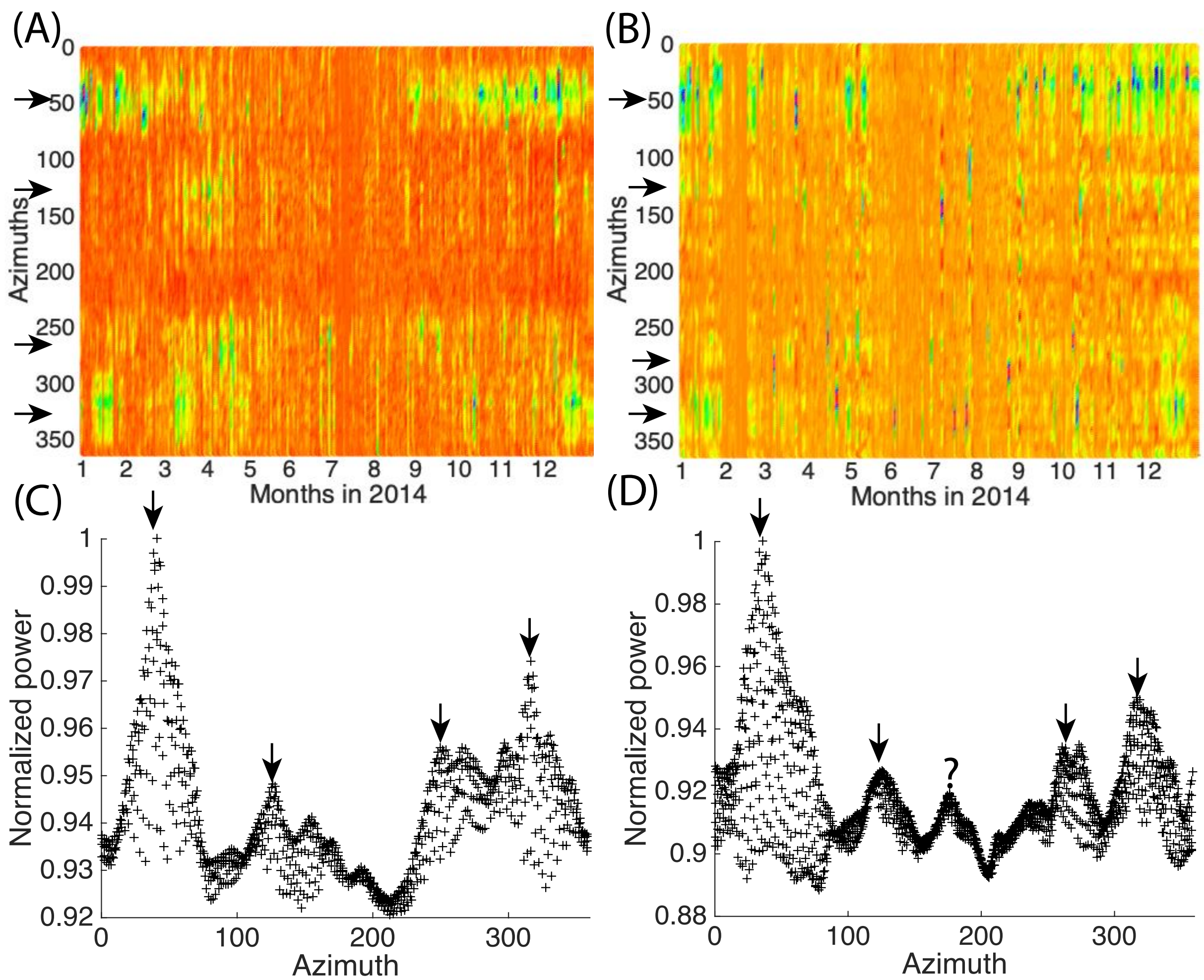

Figure 9. Seasonal variations of power spectra for primary (AC) and secondary (BD) microseisms with azimuth. Power spectra with the slowness between 0.27 and 0.35 s/km are binned based on the azimuths, from 0° to 360° with 2° interval. In each bin, we remove mean and use maximum to represent the power. Four major azimuths, ~50°, ~125°, ~260°, and ~320°, can be identified. A slight difference, ~255° for Rayleigh primary and ~270° for Rayleigh secondary, might indicate different source locations.

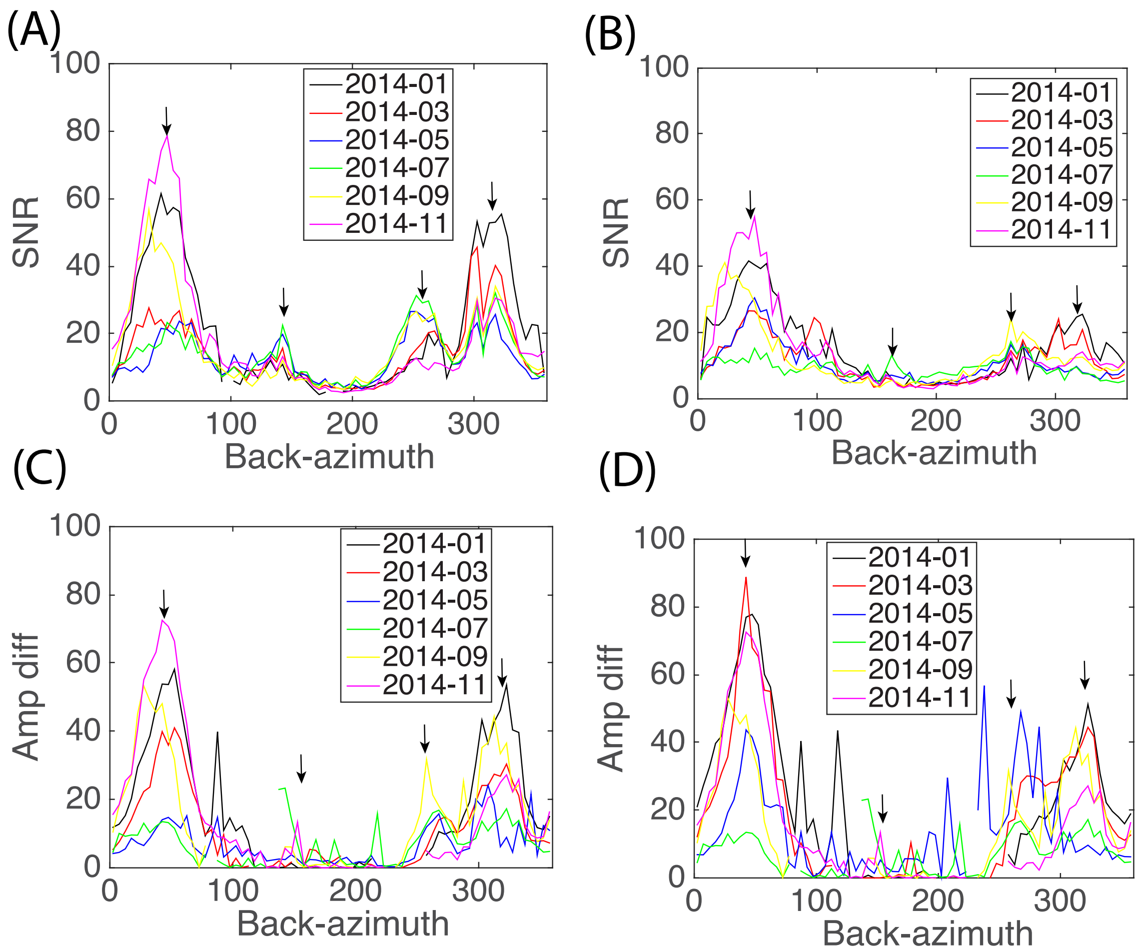

Figure 10. Seasonal variations of monthly average SNRs and amplitude difference for Rayleigh primary (AC) and secondary (BD) microseisms. Four major azimuths, 40°, 140°, 260° and 320°, are observed in the azimuthal distribution of primary and secondary microseisms. A small difference, $\sim\mathbf{255}$° for Rayleigh primary and $\sim\mathbf{270}$° for Rayleigh secondary, can also be observed. For noise with back-azimuths of $\sim\mathbf{140}$° and $\sim\mathbf{260}$°, average SNRs and amplitude difference from May to September are higher than those from November to March. For noise with back-azimuths of $\sim\mathbf{40}$° and $\sim\mathbf{320}$°, average SNRs and amplitude difference from September to March are higher than those from May to July.

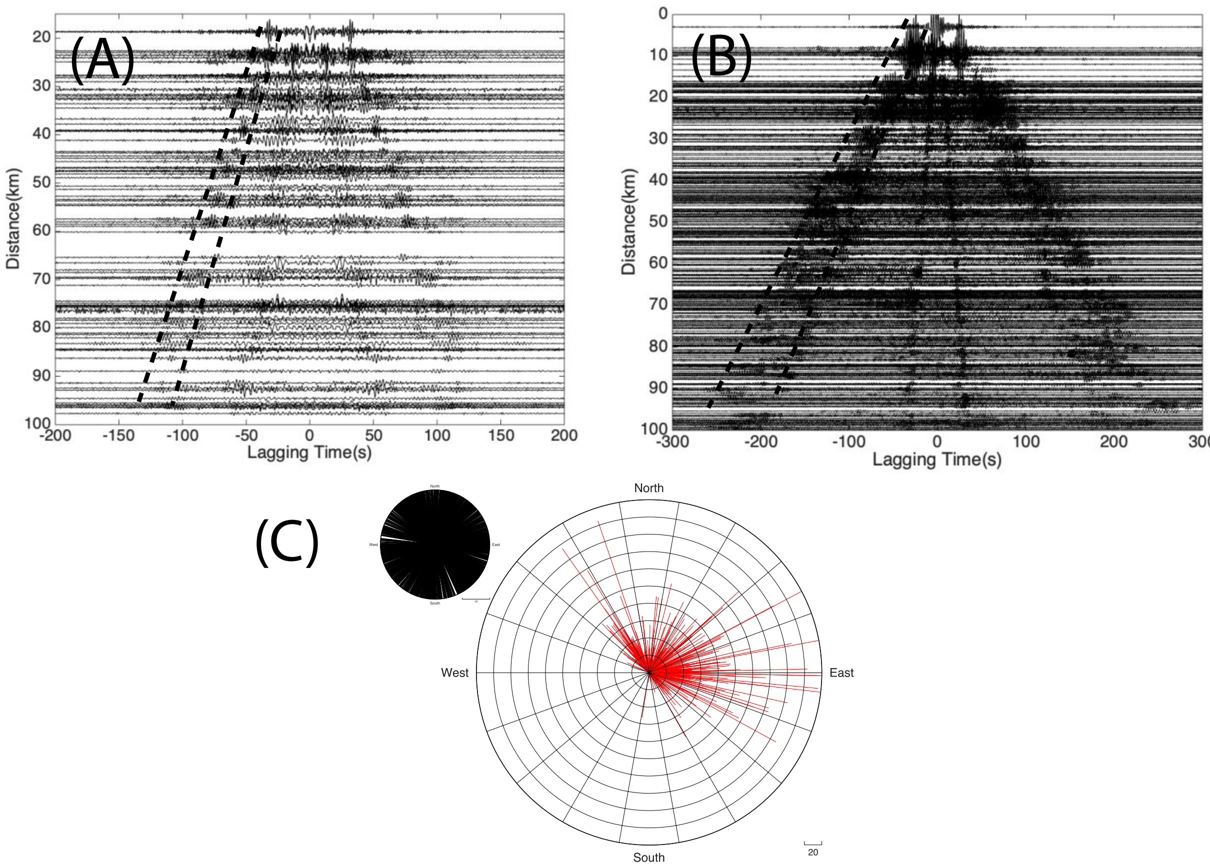

Figure 11. Directionality of sedimentary Love waves. (A) ZZ component cross-correlations showing arrivals of sedimentary Rayleigh waves (~ 0.75 km/s) within 100 km interstation distance. Sedimentary surface wave arrivals are marked between two dashed lines. (B) Arrivals of sedimentary Love waves (~ 0.45 km/s). (C) Azimuthal distribution of amplitude difference of sedimentary Love waves. No large magnitude SNRs can be observed in the third quadrant of the rose diagram. Comparing the geometry of edge of the ME and the azimuthal distribution of amplitude difference, we suggest that the generation of sedimentary Love waves is related to the basin-edge.

502

Table 1: comparison of back-azimuths from different methods

Methods	Back-azimuth1	Back-azimuth2	Back-azimuth3	Back-azimuth4
Gaussian fitting of SNRs (Rayleigh primary)	$41° \pm 17°$	N/A	$262° \pm 17°$	$317° \pm 16°$
Gaussian fitting (Rayleigh secondary)	$33° \pm 34°$	$115° \pm 17°$	$271° \pm 15°$	$324° \pm 21°$
Gaussian fitting (Love primary)	$44° \pm 19°$	$121° \pm 19°$	$269° \pm 19°$	$320° \pm 16°$
Gaussian fitting (Love secondary)	$47° \pm 17°$	N/A	$265° \pm 20°$	$322° \pm 11°$
Seasonal variations (SNR and amplitude difference, Rayleigh primary)	$\sim 40°$	$\sim 140°$	$\sim 260°$	$\sim 320°$
Seasonal variations (Rayleigh secondary)	$\sim 40°$	$\sim 150°$	$\sim 270°$	$\sim 320°$
2D FK power spectra (Primary)	$\sim 45°$	$\sim 125°$	$\sim 255°$	$\sim 320°$
2D FK power spectra (secondary)	$\sim 45°$	$\sim 125°$	$\sim 270°$	$\sim 320°$

503

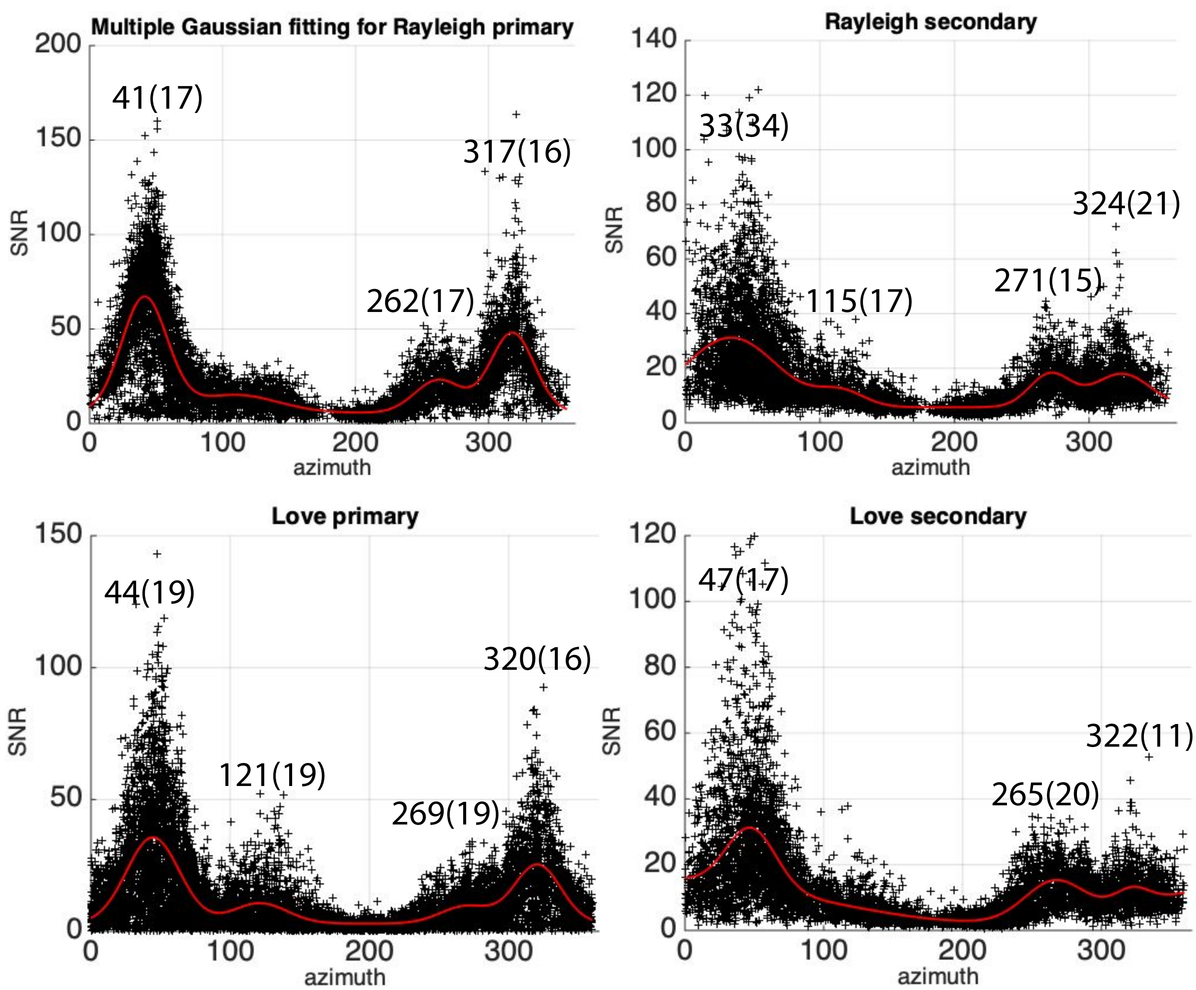

Figure 12. Multiple Gaussian function fitting for azimuthal distribution of SNR measurements. Values over local peaks of fitting curves are Gaussian means and standard deviations.

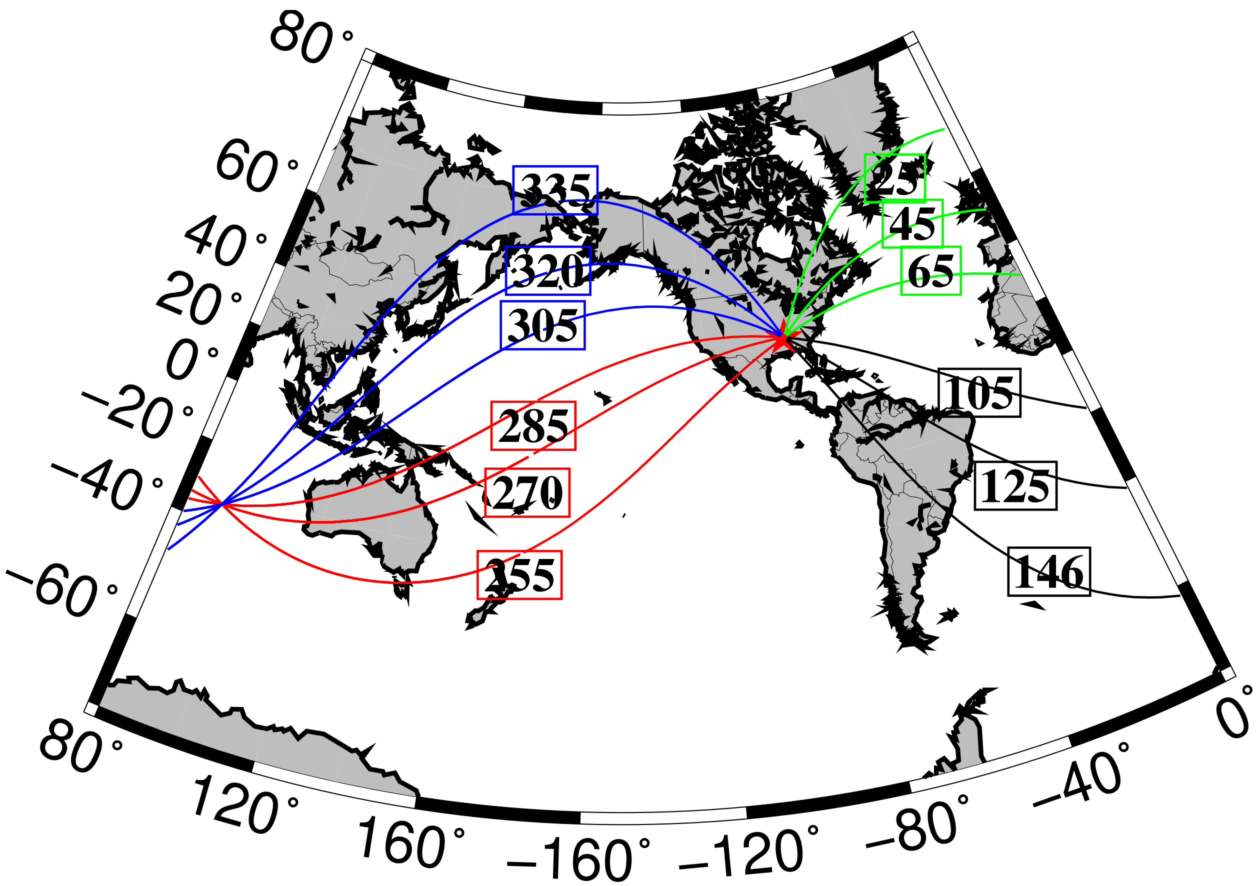

Figure 13. Source locations from back-projections with different back-azimuths. For energy flux from the back-azimuth of 45°, noise sources can be along the coast of Newfoundland or Greenland for primary microseisms and in the deep water of south of Greenland for secondary microseisms. Noise sources are along the coasts of South America for primary microseisms with the back-azimuth of 125° but in the southern Atlantic Ocean for secondary microseisms. For primary microseisms with the back-azimuth of 255°, noise source can along the coasts of Australia or New Zealand. For secondary microseisms with the back-azimuth of 270°, sources are in the southern Pacific Ocean. Noise sources for primary microseisms with the back-azimuth of 320° can along the coasts of Alaska and Canada. The secondary microseisms can originate along the coasts and related to the coastal reflections or in the deep Pacific Ocean.

References

Amante, C. & Eakins, B. W. (2009). Etopo1 arc-minute global relief model: procedures, data sources and analysis. Boulder, Colo, U.S. Dept. of Commerce, National Oceanic and Atmospheric Administration, National Environmental Satellite, Data, and Information Service, National Geophysical Data Center, Marine Geology and Geophysics Division. http://purl.access.gpo.gov/GPO/gpo441.

Ardhuin, F., Stutzmann, E., Schimmel, M., & Mangeney, A. (2011). Ocean wave sources of seismic noise. *J. geophys. Res.: Oceans*, **116**(C9), doi: 10.1029/2011JC006952.

Aki, K., & Richards, P. G. (2002). Quantitative seismology. Sausalito, Calif, University Science Books.

Behr, Y., Townend, J., Bowen, M., Carter, L., Gorman, R., Brooks, L., & Bannister, S. (2013). Source directionality of ambient seismic noise inferred from three-component beamforming. *J. geophys. Res.: Solid Earth*, **118**(1):240–248, doi: 10.1029/2012JB009382

Bensen, G., Ritzwoller, M., Barmin, M., Levshin, A., Lin, F., Moschetti, M., Shapiro, N., & Yang, Y. (2007). Processing seismic ambient noise data to obtain reliable broadband surface wave dispersion measurements. *Geophys. J. Int*., **169**(3):1239–1260, doi: 10.1111/j.1365-246X.2007.03374. x.

Brenguier, F., Campillo, M., Hadziioannou, C., Shapiro, N., Nadeau, R. M., & Larose, E. (2008a). Postseismic relaxation along the San Andreas fault at Parkfield from continuous seismological observations. *Science*, **321**(5895):1478–1481, doi: 10.1126/science.1160943.

Brenguier, F., Shapiro, N. M., Campillo, M., Ferrazzini, V., Duputel, Z., Coutant, O., & Nercessian, A. (2008b). Towards forecasting volcanic eruptions using seismic noise. *Nature Geoscience*, **1**(2):126, doi: 10.1038/ngeo104.

Bromirski, P. D., & Duennebier, F. K. (2002). The near-coastal microseism spectrum: Spatial and temporal wave climate relationships. *J. geophys. Res.: Solid Earth*, **107**(B8), ESE-5, doi: 10.1029/2001JB000265.

Burtin, A., Bollinger, L., Vergne, J., Cattin, R., &Nábělek, J. (2008). Spectral analysis of seismic noise induced by rivers: A new tool to monitor spatiotemporal changes in stream hydrodynamics. *J. geophys. Res.: Solid Earth*, **113**(B5), doi: 10.1029/2007JB005034.

Capon, J., Bolt, B. A., Alder, B., I'ernbach, S., & Rotenberg, M. (1973). Signal processing and frequency-wavenumber spectrum analysis for a large aperture seismic array. *Methods in Computational Phys.* (Elsevier, 1973), 13, 1-59, doi: 10.1016/B978-0-12-460813-9.50007-2.

Cessaro, R. K. (1994). Sources of primary and secondary microseisms. *Bull. Seism. Soc. Am.*, **84**(1), 142-148.

Chen, C., Gilbert, H., Andronicos, C., Hamburger, M. W., Larson, T., Marshak, S., & Yang, X. (2016). Shear velocity structure beneath the central United States: implications for the origin of the Illinois Basin and intraplate seismicity. *Geochem. Geophys. Geosyst.,* **17**(3), 1020-1041.

Dart, R. L. (1992). Catalog of pre-Cretaceous geologic drill-hole data from the upper Mississippi Embayment: a revision and update of open file report 90-260. USGS *Technical report*, US Dept. of the Interior, US Geological Survey.

Dart, R. L. & Swolfs, H. S. (1998). Contour mapping of relic structures in the Precambrian basement of the Reelfoot rift, North American midcontinent. *Tectonics*, **17**(2):235–249.

Derode, A., Larose, E., Campillo, M., & Fink, M. (2003). How to estimate the greens function of a heterogeneous medium between two passive sensors? Application to acoustic waves. *Appl. Phys. Lett.*, **83**(15):3054–3056.

Dumouchel, W., & O'Brien, F. (1989, April). Integrating a robust option into a multiple regression computing environment. In Computer science and statistics: *Proceedings of the 21st symposium on the interface* (pp. 297-302). American Statistical Association Alexandria, VA.

Duputel, Z., Ferrazzini, V., Brenguier, F., Shapiro, N., Campillo, M., & Nercessian, A. (2009). Real time monitoring of relative velocity changes using ambient seismic noise at the Piton de la Fournaise volcano (La Réunion) from January 2006 to June 2007. *Journal of Volcanology and Geothermal Res.*, **184**(1-2):164–173.

Field, E. H. (1996). Spectral amplification in a sediment-filled valley exhibiting clear basin-edge-induced waves. *Bull. Seism. Soc. Am.*, **86**(4):991–1005.

Fu, Y. V. & Li, A. (2015). Crustal shear wave velocity and radial anisotropy beneath the Rio Grande rift from ambient noise tomography. *J. geophys. Res.: Solid Earth*, **120**(2):1005–1019.

Furumura, M. & Sasatani, T. (1996). Secondarily generated surface waves in the Tokachi basin, Hokkaido, Japan. *J. of Phys. of the Earth*, **44**(2):115–132.

Gerstoft, P., Shearer, P. M., Harmon, N., & Zhang, J. (2008). Global P, PP, and PKP wave microseisms observed from distant storms. *Geophys. Res. Lett.*, **35**(23).

Gu, Y. J., Dublanko, C., Lerner-Lam, A., Brzak, K., & Steckler, M. (2007). Probing the sources of ambient seismic noise near the coasts of southern Italy. *Geophys. Res. Lett.*, **34**(22).

Gu, Y. J. & Shen, L. (2012). Microseismic noise from large ice-covered lakes? *Bull. Seism. Soc. Am.*, **102**(3):1155–1166.

Harmon, N., Rychert, C., & Gerstoft, P. (2010). Distribution of noise sources for seismic interferometry. *Geophys. J. Int.*, **183**(3):1470–1484.

Hasselmann, K. (1963). A statistical analysis of the generation of microseisms. *Rev. Geophys.,* **1**(2):177–210.

Hatayama, K., Matsunami, K., Iwata, T., & Irikura, K. (1995). Basin-induced love waves in the eastern part of the Osaka basin. *J. of Phys. of the Earth*, **43**(2):131–155.

Hildenbrand, T. G., & Hendricks, J. D. (1995). Geophysical setting of the Reelfoot rift and relations between rift structures and the New Madrid seismic zone. USGS *Technical report*, No. 1538-E, US Geological Survey, doi: 10.3133/pp1538E.

Hillers, G., Ben-Zion, Y., Campillo, M., & Zigone, D. (2015). Seasonal variations of seismic velocities in the San Jacinto fault area observed with ambient seismic noise. *Geophys. J. Int.*, **202**(2):920–932.

Holland, P. W., & R. E. Welsch. "Robust Regression Using Iteratively Reweighted Least-Squares." *Comm. in Statistics: Theory and Methods*, A6, 1977, pp. 813–827, doi: 10.1080/03610927708827533.

Joyner, W. B. (2000). Strong motion from surface waves in deep sedimentary basins. *Bull. Seism. Soc. Am.*, **90**(6B): S95–S112.

Kawase, H. (1996). The cause of the damage belt in Kobe: The basin-edge effect, constructive interference of the direct S-wave with the basin-induced diffracted/Rayleigh waves. *Seism. Res. Lett.*, **67**(5):25–34.

Kedar, S., Longuet-Higgins, M., Webb, F., Graham, N., Clayton, R., & Jones, C. (2008). The origin of deep ocean microseisms in the north Atlantic Ocean. *Proc. R. Soc. A.* **464**(2091):777–793.

Kibblewhite, A. C. and Ewans, K. C. (1985). Wave–wave interactions, microseisms, and infrasonic ambient noise in the ocean. *J. Acous. Soc. of Am.*, **78**(3):981– 994.

Landès, M., Hubans, F., Shapiro, N. M., Paul, A., & Campillo, M. (2010). Origin of deep ocean microseisms by using teleseismic body waves. *J. geophys. Res.: Solid Earth*, **115**(B5).

Langston, C. A., Bodin, P., Powell, C., Withers, M., Horton, S., & Mooney, W. (2005). Bulk sediment Q_p and Q_s in the Mississippi embayment, central United States. *Bull. Seism. Soc. Am.*, **95**(6), 2162-2179.

Langston, C. A., Chiu, S.-C. C., Lawrence, Z., Bodin, P., & Horton, S. (2009). Array observations of microseismic noise and the nature of H/V in the Mississippi embayment. *Bull. Seism. Soc. Am.*, **99**(5):2893–2911.

Lecocq, T., Caudron, C., & Brenguier, F. (2014). MSNoise, a python package for monitoring seismic velocity changes using ambient seismic noise. *Seism. Res. Lett.*, **85**(3):715–726.

Liang, C. & Langston, C. A. (2008). Ambient seismic noise tomography and structure of eastern North America. *J. geophys. Res.: Solid Earth*, **113**(B3).

Liang, C. & Langston, C. A. (2009). Three-dimensional crustal structure of eastern North America extracted from ambient noise. *J. geophys. Res.: Solid Earth*, **114**(B3).

Lin, F.-C., Li, D., Clayton, R. W., & Hollis, D. (2013). High-resolution 3D shallow crustal structure in Long Beach, California: Application of ambient noise tomography on a dense seismic array noise tomography with a dense array. *Geophysics*, **78**(4): Q45–Q56.

Lin, F. C., Moschetti, M. P., & Ritzwoller, M. H. (2008). Surface wave tomography of the western United States from ambient seismic noise: Rayleigh and love wave phase velocity maps. *Geophys. J. Int.*, **173**(1):281–298.

Lin, F. C., Ritzwoller, M. H., Townend, J., Bannister, S., & Savage, M. K. (2007). Ambient noise Rayleigh wave tomography of New Zealand. *Geophys. J. Int.*, **170**(2):649– 666.

Liu, C., Langston, C. A., Powell, C. A., & Cramer, C. H. (2018, December). Near Surface to Upper Mantle Velocity Structure in the Mississippi Embayment from Ambient Noise Tomography. In *AGU Fall Meeting Abstracts*.

Liu, Z., Huang, J., He, P., & Qi, J. (2018b). Ambient noise monitoring of seismic velocity around the Longmen Shan fault zone from 10 years of continuous observation. *J. geophys. Res.: Solid Earth*, **123**(10):8979–8994.

Longuet-Higgins, M. S. (1950). A theory of the origin of microseisms. Philosophical Transactions of the Royal Society of London. Series A, *Mathematical and Phys. Sciences*, **243**(857):1–35.

Meier, U., Shapiro, N. M., & Brenguier, F. (2010). Detecting seasonal variations in seismic velocities within Los Angeles basin from correlations of ambient seismic noise. *Geophys. J. Int.*, **181**(2):985–996.

Nakata, N., Chang, J. P., Lawrence, J. F., & Boué, P. (2015). Body wave extraction and tomography at Long Beach, California, with ambient-noise interferometry. *J. geophys. Res.: Solid Earth*, **120**(2):1159–1173.

Narayan, J. P. (2012). Effects of P-wave and S-wave impedance contrast on the characteristics of basin transduced Rayleigh waves. *Pure Appl. Geophys.*, **169**(4), 693-709.

Nishida, K., Montagner, J. P., & Kawakatsu, H. (2009). Global surface wave tomography using seismic hum. *Science*, **326**(5949):112–112.

Niu, F., Silver, P. G., Daley, T. M., Cheng, X., & Majer, E. L. (2008). Preseismic velocity changes observed from active source monitoring at the Parkfield SAFOD drill site. *Nature*, **454**(7201):204.

Reading, A. M., Koper, K. D., Gal, M., Graham, L. S., Tkalčić, H., & Hemer, M. A. (2014). Dominant seismic noise sources in the Southern Ocean and West Pacific, 2000–2012, recorded at the Warramunga Seismic Array, Australia. *Geophys. Res. Lett.*, **41**(10), 3455-3463.

Retailleau, L., Boué, P., Stehly, L., & Campillo, M. (2017). Locating microseism sources using spurious arrivals in intercontinental noise correlations. *J. geophys. Res.: Solid Earth*, **122**(10), 8107-8120.

Ritzwoller, M. H., Shapiro, N. M., Barmin, M. P., & Levshin, A. L. (2002). Global surface wave diffraction tomography. *J. geophys. Res.: Solid Earth*, **107**(B12)

Rovelli, A., Scognamiglio, L., Marra, F., & Caserta, A. (2001). Edge-diffracted 1-sec surface waves observed in a small-size intramountain basin (Colfiorito, Central Italy). *Bull. Seism. Soc. Am.*, **91**(6):1851–1866.

Seber, G. A. F., & C. J. Wild. Nonlinear Regression. Hoboken, NJ: *Wiley-Interscience*, 2003, http://site.ebrary.com/id/10275079.

Sens-Schönfelder, C. & Wegler, U. (2006). Passive image interferometry and seasonal variations of seismic velocities at Merapi volcano, Indonesia. *Geophys. Res. Lett.*, **33**(21).

Shapiro, N. M., Ritzwoller, M., & Bensen, G. (2006). Source location of the 26 sec microseism from cross-correlations of ambient seismic noise. *Geophys. Res. Lett.*, **33**(18).

Silver, P. G., Daley, T. M., Niu, F., & Majer, E. L. (2007). Active source monitoring of cross-well seismic travel time for stress-induced changes. *Bull. Seism. Soc. Am.*, **97**(1B):281–293.

Snieder, R. (2004). Extracting the greens function from the correlation of Coda waves: A derivation based on stationary phase. *Phys. Rev. E*, **69**(4):046610.

Stehly, L., Campillo, M., & Shapiro, N. (2006). A study of the seismic noise from its long-range correlation properties. *J. geophys. Res.: Solid Earth*, **111**(B10).

Tian, Y. & Ritzwoller, M. H. (2015). Directionality of ambient noise on the Juan de Fuca plate: Implications for source locations of the primary and secondary microseisms. *Geophys. J. Int*., **201**(1):429–443.

Tsai, V. C. (2009). On establishing the accuracy of noise tomography travel-time measurements in a realistic medium. *Geophys. J. Int*., **178**(3):1555–1564.

Wapenaar, K. (2004). Retrieving the elastodynamic Green's function of an arbitrary inhomogeneous medium by cross correlation. *Phys. Rev. Lett*., **93**(25):254301.

Weaver, R., Froment, B., & Campillo, M. (2009). On the correlation of non-isotropically distributed ballistic scalar diffuse waves. *J. Acous. Soc. A*., **126**(4):1817–1826.

Weaver, R. L. & Lobkis, O. I. (2001). Ultrasonics without a source: Thermal fluctuation correlations at MHz frequencies. *Phys. Rev. Lett*., **87**(13):134301.

Wiechert, E., 1904. Discussion, Verhandlung der zweiten Internationalen Seismologischen Konferenz, *Beitrage Zur Geophys*., **2**, 41-43.

Wu, C., Delorey, A., Brenguier, F., Hadziioannou, C., Daub, E. G., & Johnson, P. (2016). Constraining depth range of S wave velocity decrease after large earthquakes near Parkfield, California. *Geophys. Res. Lett*., **43**(12):6129–6136.

Yang, Y. & Ritzwoller, M. H. (2008). Characteristics of ambient seismic noise as a source for surface wave tomography. *Geochem. Geophys. Geosyst.*, **9**(2).

Yao, H. & Van Der Hilst, R. D. (2009). Analysis of ambient noise energy distribution and phase velocity bias in ambient noise tomography, with application to SE Tibet. *Geophys. J. Int*., **179**(2):1113–1132.

Yao, H., van Der Hilst, R. D., & De Hoop, M. V. (2006). Surface-wave array tomography in SE Tibet from ambient seismic noise and two-station analysis: I-phase velocity maps. *Geophys. J. Int*., **166**(2):732–744.

Young, I. (1999). Seasonal variability of the global ocean wind and wave climate. *Int. J. of Climatology*, **19**(9):931–950.

Zeng, X. & Ni, S. (2010). A persistent localized microseismic source near the Kyushu island, japan. *Geophys. Res. Lett.,* **37**(24).